Theoretical and Experimental Characterization of a Near-Field Scanning Microwave (NSMM)

W. Charles Symons, III, *Member, IEEE*, Keith W. Whites, *Senior Member, IEEE*, and Robert A. Lodder

***Abstract*—An important aspect to understanding near-field optics and imaging involves the electromagnetic scattering characteristics of objects illuminated by the near field of a sub-wavelength-sized aperture. This paper addresses one particular application of near-field optics: a transmission-mode near-field scanning microscope (NSM). Specifically, some peculiar phenomena are investigated including a near-field focusing effect, as well as an impedance-based image-shape effect. To this end, we first describe the physical attributes of an NSM and then present two computational models we use to characterize this instrument. Both moment-method and finite-difference time-domain models are discussed. These two models are applied to the analysis of the NSM for various configurations and compared to other theoretical and experimental results. Finally, the construction of an *X*-band NSM is described—which we label a near-field scanning microwave microscope—and the experimental near-field imaging measurements are compared with our numerical predictions.**

***Index Terms*—Finite-difference time-domain (FDTD) method, moment method (MM), near-field imaging, near-field scanning microscopy, near-field scanning microwave microscope (NSMM), near-field scanning optical microscope (NSOM), thin wires.**

I. Introduction

NANOMETER-SIZED structures are becoming increasingly important and, as a result, near-field scanning optical microscopes (NSOMs) are becoming increasingly popular analytical tools [1]. An NSOM instrument allow samples that are smaller than half the wavelength of light to be imaged by using an aperture size and an aperture-sample separation distance that is less than a wavelength of the source. Furthermore, because optical sources are utilized, NSOM instruments provide this resolution while maintaining the advantages of traditional optical microscopes including nondestructive sample analysis, as well as spectroscopic analysis.

In order to gain a better understanding of near-field scanning microscopes (NSMs), both moment-method (MM) and finite-difference time-domain (FDTD) numerical techniques have been implemented to study this near-field scattering problem. While our models provided interesting insight into the NSM instrument, they require the use of certain assumptions to make them tractable. These assumptions include imaging an electrically thin wire, as well as placing the NSM aperture within an infinite perfectly electrically conducting (PEC) plate. While other models have been developed for studying NSOM instruments [2]–[6], our models differ in both their implementation and imaging phenomena being investigated. Consequently, in addition to these computational models, a near-field scanning microwave microscope (NSMM) has been constructed for use in comparing experimental measurements from this instrument with our numerical predictions. To this end, our models and the experimental setup are designed to be as similar as possible in order to eliminate variations and, therefore, achieve the most accurate results.

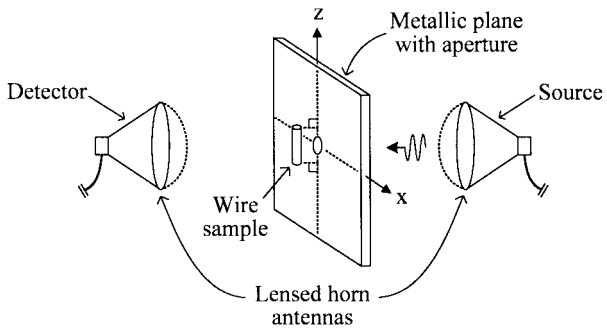

Fig. 1. NSM arrangement

A. Physical Setup

There are three basic configurations in which scattering-type NSM instruments appear [1], [7]. All three configurations share a sub-wavelength aperture that is placed within a wavelength of the sample. The resolution of the instrument is dependent on the aperture size, source–sample separation distance, and scanning step size. NSMs can use the aperture as a source, detector, or both. For this paper, the physical NSM instrument to be studied is a transmission-mode microscope, as illustrated in Fig. 1, wherein the sub-wavelength aperture is placed very near the sample and raster scanned, while a detector behind the sample collects the transmitted signal.

Our first NSM instrument was a near-infrared (near-IR) NSOM where the source was tunable from approximately 1730 to 1780 nm [8]. In order to theoretically model this complex instrument, several simplifications were made. First, while the majority of NSOM instruments—including our near-IR NSOM—incorporate a modified fiber-optic probe as the source, this paper will concentrate on a simpler design. Specifically, as depicted in Fig. 1, the aperture under consideration is a

Manuscript received June 18, 2001; revised January 25, 2002. This work was supported by the University of Kentucky Medical Center Research Fund, by the University of Kentucky Center for Computational Sciences, and by the National Science Foundation under the Faculty Early Career Development (CAREER) Award ECS-9624486.

W. C. Symons, III is with the Bradley Department of Electrical and Computer Engineering, Virginia Polytechnic Institute, Blacksburg, VA 24061-0111 USA.

K. W. Whites is with the Department of Electrical and Computer Engineering, South Dakota School of Mines and Technology, Rapid City, SD 57701-3995 USA.

R. A. Lodder is with the College of Pharmacy, University of Kentucky, Lexington, KY 40506-0286 USA.

Digital Object Identifier 10.1109/TMTT.2002.806915

sub-wavelength hole within a large metallic plate. In order to obtain an image, the aperture is scanned point-by-point in a plane close behind the sample.

Second, for simplicity, the sample was chosen to be a metallic thin wire. In fact, this is not much different from actual characterization of NSOM instruments using gratings [9]–[11]. Specifically, thin-wire samples allow for easy characterization of NSM instruments. For example, the resolution of the instrument can be determined based on the wire length and diameter. Polarization effects can also be readily characterized using thin-wire samples. Furthermore, during the course of our modeling of the NSM instrument, unexpectedly shaped NSM images and certain enhancement effects were observed. We found that these effects were more easily explained and characterized using a thin-wire sample.

II. Computational Models

We developed two computational models to numerically model the performance of the NSOM instrument. Specifically, MM and FDTD models were utilized. Both of these were based upon the simple physical setup discussed previously containing an aperture and a thin wire, as illustrated in Fig. 1. The sub-wavelength aperture is assumed to exist in an infinite PEC plane. Furthermore, both models used PEC thin wires as the sample to be studied and imaged. One of the main differences between the MM and FDTD models involved the sources. Our MM model used a constant magnetic surface current density within the aperture, while the FDTD model used a current sheet excitation, providing an incident wave on the nonsample side of the aperture. Each of these models is briefly discussed below.

A. MM Model

For the MM model, the induced thin-wire current was expanded in a set of triangle sub-domain basis functions and tested with pulse functions in the standard fashion [12], [13]. To incorporate the source of the NSOM instrument, we use a simplistic model of the fields in the aperture that turns out to be most satisfactory for our purposes. In particular, we assume that electric field $\overline{E}$ in the aperture is constant and much larger than the scattered $\overline{E}$. Assuming $\overline{E}$ within the aperture is known, the aperture can be replaced by an equivalent magnetic current source $\overline{M}_s$ [14]. Image theory allows the infinite PEC plane to be removed by imaging the source and specimen. This imaging leaves a magnetic current source $2\overline{M}_s$ and an imaged specimen with oppositely directed currents from the actual specimen.

It is important to note that this specific aperture model is only an approximation. By assuming a constant electric field within the aperture, this source model ignores the mutual coupling between the source and specimen. However, because NSM imaging is a relative effect based upon aperture location, this simple model should give reasonably accurate results. As it turns out, this does appear to be the case, as will be seen later in Figs. 10 and 11 when NSM images from this method, the FDTD method, and experimental measurements are compared.

Proceeding with this aperture model and employing a source–field relationship, the incident electric field can be computed as [14]

$$\overline{E}^i = \int_{\text{aperture}} \left\{ -\hat{x}\left(2E_{ax}\frac{dg}{dy}\right) + 2\hat{y}\left(E_{az}\frac{dg}{dz} + E_{ax}\frac{dg}{dx}\right) - \hat{z}\left(2E_{az}\frac{dg}{dy}\right)\right\} ds \quad (1)$$

where E_{ax} and E_{az} are the x- and z-directed components of the electric field in the aperture, respectively, and g is the time–harmonic free-space Green's function

$$g = \frac{e^{-jkR}}{4\pi R} \quad (2)$$

with an $e^{j\omega t}$ time convention and wavenumber k, where

$$R = \sqrt{(x-x')^2 + (y-y')^2 + (z-z')^2}. \quad (3)$$

After simplification of (1), the incident electric field produced by a constant electric field in the aperture is given as

$$\overline{E}^i = \hat{z}2\pi a^2 E_{az}(y-y')\frac{1+jkR}{4\pi R^3}e^{-jkR} \quad (4)$$

for the aperture orientation shown in Fig. 1, where a is the radius of the aperture that is located in the xz-plane, and with the wire oriented in the z-direction.

With this source model and the fact that the specimen is imaged, there are twice as many wires in the equivalent problem as in the original problem. An image plane thin-wire kernel simultaneously representing both a specimen wire and its image was used as follows:

$$G_{\text{tw}} = \frac{e^{-jkR_1}}{4\pi R_1} - \frac{e^{-jkR_2}}{4\pi R_2} \quad (5)$$

where R_1 is the distance from the current on the wire to the observation point on the wire and R_2 is the distance from that same current to the corresponding observation point on the image wire.

The system of equations resulting from the MM basis function expansion and testing can be written in the form

$$[z_{mn}][\alpha_n] = [g_m] \quad (6)$$

where $[z_{mn}]$ is the impedance matrix, $[\alpha_n]$ is the vector of unknown thin-wire current coefficients, and $[g_m]$ is the excitation vector due to the $2\overline{M}_s$. With this MM model, simulating the NSM raster scan is as simple as relocating the $2\overline{M}_s$ magnetic current disk and recomputing the incident electric field. Of course, before this raster scanning, the impedance matrix $[z_{mn}]$ was computed once and decomposed so that the currents could be computed by simply backsubstituting the LU decomposed impedance matrix with the new excitation vector. Our simulated NSM image was obtained by computing the detected power received at a point 100 λ (λ = free-space wavelength) directly behind the center of the wire. Specifically, this detected power was computed from the $2\overline{M}_s$ magnetic current disk, the currents on the wire specimens, and their respective images.

Incidentally, the excitation vector described above can introduce a convergence anomaly into the MM solution depending

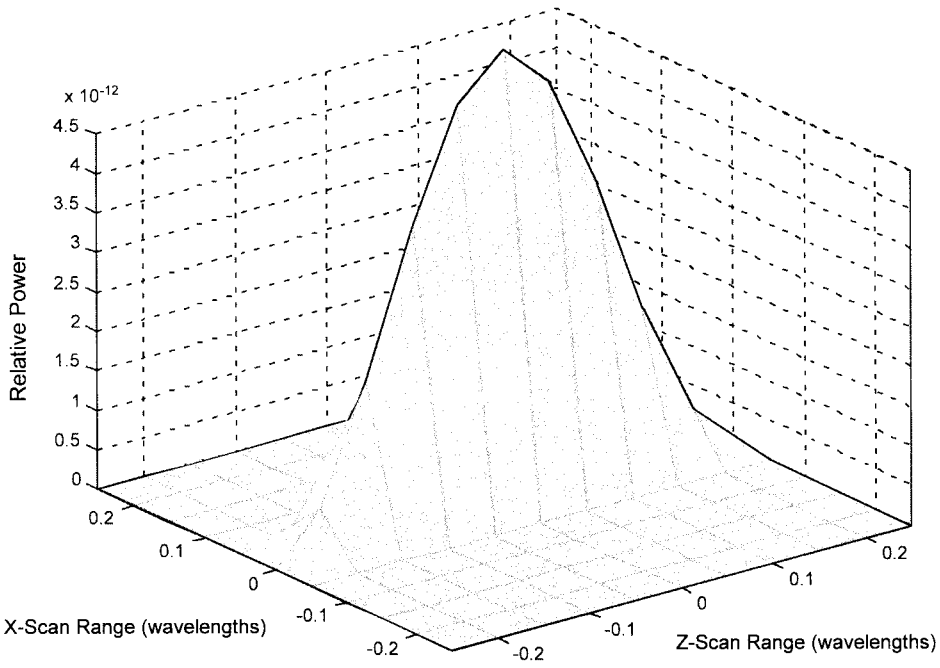

Fig. 2. MM predicted near-field scanning image for a thin wire of length 1.5 cm and radius 0.03 mm using an 11 × 11 grid of observation points near the $\lambda/2$ resonance ($f = 10\,\text{GHz}$)

on the level of approximation used in the evaluation of the elements. For example, using a simple point-match evaluation is not recommended since $\overline{E}^i$ can be rapidly varying over the segments of the wire model when the $2\overline{M}_s$ current disk is close to the wire, which is the normal operating conditions for NSM. On the other hand, the straightforward numerical integration of (4) was generally found to be too time consuming for a complete raster scanned image. A compromise for the efficient and accurate evaluation of the excitation vector was to compute the incident field at a large number of preselected points along the wire. The testing integration of $\overline{E}^i$ was then performed analytically using a linearly interpolated incident electric field. Due to this analytical integration, a converged excitation vector and current solution could be obtained while minimizing the computational time to fill the excitation vector in (6).

Naturally, an important test of this MM code is to verify that it can actually produce a sub-wavelength image of a specimen. For this test, a 0.5-λ-long wire with radius 0.001 λ was selected. The "probe" ($2\overline{M}_s$ current disk) was scanned 0.25 λ within a plane from the center of the wire in an 11 × 11 grid. The numerically generated NSM image of this wire is shown in Fig. 2 and confirms the sub-wavelength resolution of the NSM. The probe had an aperture radius of 0.001 λ and was kept 0.005 λ from the specimen. The polarization of the electric field within the aperture was totally z directed and had a strength of 1 V/m.

Note that we selected the length of this wire to be near resonance. It was important for us to produce images at or near resonance in order to make comparisons with the X-band NSMM instrument, described later in Section III. Resonance was chosen because it is an easily identifiable spectral location, particularly given that this instrument becomes quite noisy away from resonance. It is important to emphasize that the noise does not make imaging impossible, but it is relatively simpler to compare the measured data to numerical data at a specified spectral point such as resonance.

B. Near-Field Focusing Effect

One particularly noteworthy aspect of the image in Fig. 2 is that the detected power is actually largest when the source is positioned directly *behind* the wire and covers up the aperture. This appears to be a near-field focusing effect not seen in other models that image larger specimens [2], [15], [16]. However, at least one physical NSOM instrument [10] has obtained transmission images where the specimen appears brighter than the background, as in our computer-generated NSM image. We also show later that this near-field focusing phenomenon exists experimentally utilizing an X-band NSMM instrument.

C. Impedance-Based Shape Effect

Another interesting phenomenon in the wire image of Fig. 2 is the rounded shape of the image along the length of the wire. At first glance, one may be tempted to expect a nearly constant NSM image of the wire since the aperture source "sees" a large expanse of wire regardless of its position when behind the wire—except, possibly, very near the wire ends.

In reality, however, the rounded NSM image can be attributed to the fact that the "coupling impedance" between the aperture and wire varies as the source is moved along the wire. For example, consider a $\lambda/2$-long wire containing a delta-gap voltage source [12], [17]. Utilizing a thin-wire MM code, this specimen was modeled for various positions of a delta-gap source along the wire. The impedance was measured for each source position and plotted in Fig. 3. From this figure, it is evident that the shape of the impedance plot varies inversely to the shape of the NSM wire image.

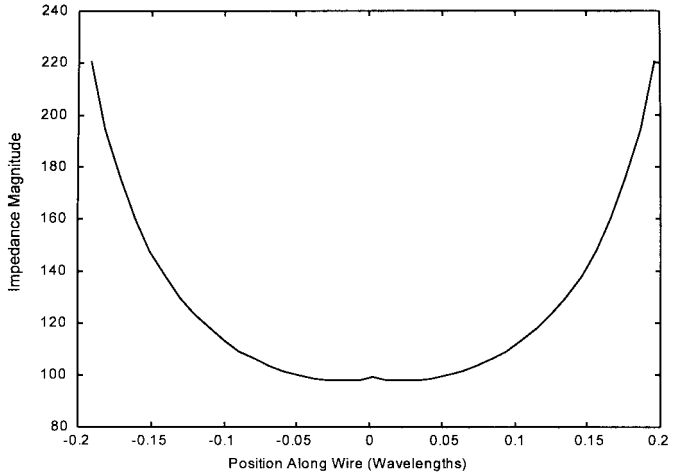

Fig. 3. Predicted impedance magnitude [Ω] along a thin wire of length 1.5 cm and radius 0.03 mm at the frequency 10 GHz for a delta-gap excitation

Obviously, the coupling impedance along the wire shown in Fig. 3 characterizes the shape of the resulting wire image shown in Fig. 2. Specifically, an increased coupling impedance results in less energy being coupled to the wire specimen. Since the energy exciting the wire is diminished, the energy radiated by the wire and subsequently received by the detector is also reduced. In this manner, the shape of the wire image is inversely proportional to the coupling impedance along the wire. Furthermore, this relationship between coupling impedance and NSM image shape leads to the conclusion that, because coupling impedance is dependent on the excitation frequency, the image shape should also vary with excitation frequency.

D. FDTD Model

We chose to also model the NSMM instrument using the FDTD method. This second computational model was used to verify the MM solution and to test the limitations of the constant $\overline{E}$-field assumption in the aperture. The traditional Yee FDTD algorithm [18] was utilized to model the NSMM instrument formed by the aperture and thin wire. The space was truncated using a second-order Higdon absorbing boundary condition [18].

The implementation of the aperture and the thin wire in the FDTD method generates a fundamental problem for a grid-based model since the sizes of these structures range over several orders of magnitude. In order to keep the coding simple and concise, the contour finite-difference time-domain (CFDTD) method [19] was chosen to implement the thin-wire sample and the sub-wavelength aperture. With CFDTD, it is important to realize that the Courant stability requirement now requires that the time step Δt satisfy

$$\Delta t \leq \frac{1}{c\sqrt{\dfrac{1}{\Delta y^2}+\dfrac{1}{r^2}+\dfrac{1}{r^2}}} \tag{7}$$

where Δy is the smallest y-directed grid spacing and r is the radius of the aperture, which is the smallest grid spacing in the x- and z-directions. In general, this stability requirement also worked well for our thin-wire model, which could require that the time step specified above be reinvestigated. In this case, the chosen time step was tested in order to verify that a stable result was obtained.

The FDTD model of the NSM differed from the MM model in one significant way. Specifically, the FDTD model utilized a current sheet excitation on the nonsample side of the aperture as opposed to the constant aperture $\overline{E}$-field. Consequently, mutual coupling between the aperture and sample could be accounted for in the FDTD model. Furthermore, the X-band NSMM, discussed below, utilized nearly an identical source. Despite the differing excitation models, both the MM and FDTD simulations of the NSM produced very similar images, as will be shown in Section III.

III. X-Band NSMM

While the vast majority of NSM instruments utilize optical wavelengths, the sample size limitations imposed by such small wavelengths make it difficult to produce specimens that exactly duplicate those being utilized in our computational simulations. To compensate for this difficulty, an X-band ($\approx$ 8–12 GHz) NSMM was designed and constructed. At the center of the X-band, the wavelength is approximately 3 cm so that specimens of resonant size are much easier to work with at these frequencies than those used with a near-IR NSOM instrument, for example.

As stated in [1], NSM instruments constructed for use in the microwave portion of the electromagnetic spectrum can serve as a bridge between NSOM theory and experimental results because of the simple fact that the NSM effect is not limited to optical frequencies, but is independent of wavelength. In fact, Ash and Nicholls [20] conducted one of the first experiments definitively proving the NSM effect. In their experiments, they imaged wire gratings at resolutions up to $\lambda/60$ at 10 GHz and produced sub-wavelength cross-sectional images of their diffraction grating. Furthermore, currently ongoing experiments also utilize larger wavelengths to test and verify NSM techniques and phenomena. For example, in a recent submission by Nozokido *et al.*, a millimeter-wave experiment was utilized to test a metal slit probe design [21].

A. X-Band NSMM Instrument Setup

Our X-band NSMM instrument shown in Fig. 4 has a simple design utilizing a square aluminum plate (33 cm $\times$34.5 cm) containing a small 0.159-cm-radius (0.0529 λ at 10 GHz) circular aperture drilled at the center of the plate. The plate was mounted on a two-axis positioning stage that allows the aperture to be centered in the focal plane of two lensed horn antennas, which were spaced approximately 61 cm apart. In order to suspend thin-wire specimens in front of the aperture with minimal electromagnetic interference, a specimen holder was created from Styrofoam and extruded polystyrene since both are nearly transparent at X-band frequencies. Fig. 5 shows a specimen wire being suspended in front of the aperture by this specimen holder. Additionally, a three-axis positioner was incorporated into the specimen holder to facilitate positioning of specimens in front of the aperture.

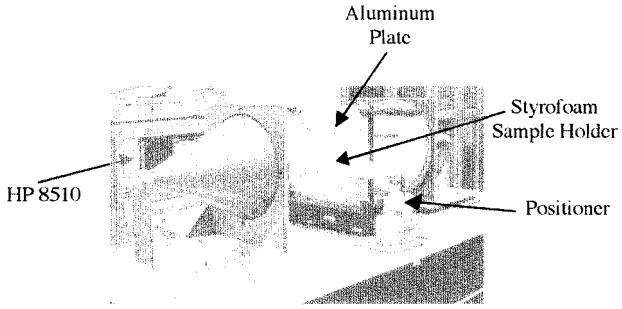

Fig. 4. X-band NSMM instrument

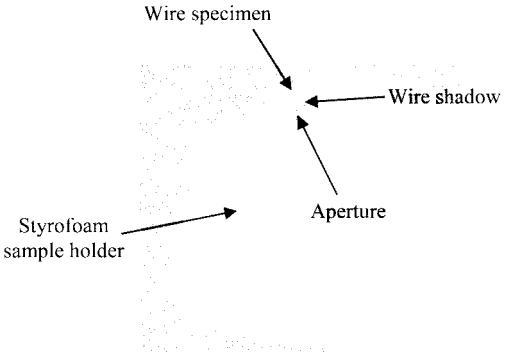

Fig. 5. Thin-wire specimen supported on a Styrofoam sample holder. The specimen is located in front of an aperture (not visible) in the metal plate

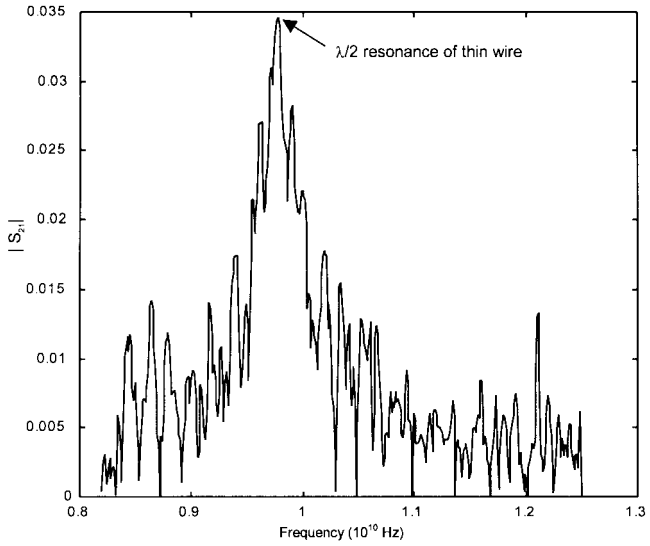

Fig. 6. Measured $|S_{21}|$ from the VNA for a 30-AWG copper wire of length 1.4 cm and radius 0.0127 cm centered over the aperture in the NSMM instrument. The sample is located 0.15 cm in front of the aperture

The X-band lensed horn antenna system with a vector network analyzer (VNA) was located in the Electromagnetic Materials Laboratory, Department of Electrical and Computer Engineering, University of Kentucky, Lexington. It was used in the past for scattering measurements of composite materials [22]. Little modifications were needed to allow it to collect X-band NSMM measurements.

In order to collect an image, the aperture must be raster scanned in a plane parallel to the specimen. Due to this scanning nature of the NSMM instrument, an aperture positioning stage was utilized to actually scan the aperture across a vertically oriented wire. Since the aperture stage was not capable of scanning the aperture vertically, the less accurate specimen holder positioner was utilized to scan the wire vertically past the aperture. In this manner, complete images could be collected.

The lensed horn antennas mentioned previously are used as both the source and detector for the X-band NSMM. Specifically, the antenna connected to port 2 is located on the opposite side of the plate as the specimen and, therefore, was generally considered the source antenna. Similarly, the antenna connected to port 1 was located on the specimen side of the aperture plate and was considered the detector antenna. In this configuration, the X-band NSMM source more closely resembles the FDTD current sheet excitation described in Section II-D than the magnetic surface current density source described in Section II-A. The lensed horn antennas were connected to a Hewlett-Packard 8510B Vector Network Analyzer, which included an 8515A S-Parameter Test Set and an 8340B Synthesized Sweeper in addition to the 8510 Network Analyzer itself.

This setup allows the complex scattering parameters S_{11}, S_{21}, S_{12}, and S_{22} to be measured over the desired range of 8.2–12.5 GHz. For the case of a transmission-mode NSMM instrument, the scattering parameter of interest was S_{12} $(= S_{21})$ since this is related to the power transmitted from the source (port 2) and received at the detector (port 1). Before utilizing the X-band NSMM setup to collect image data, a thru-reflect-line (TRL) calibration was performed, wherein the VNA was used to measure transmitted, reflected, and quarter-wavelength line signals. Once these signals were measured, the VNA then computed a set of calibration parameters, which were utilized in the collection of the image data.

B. X-Band NSMM Results

A number of experiments were developed to test the near-field focusing and other effects illustrated earlier in the MM and FDTD results. First, an appropriate wire specimen was chosen to simply test the NSMM's ability to image a thin wire. A 1.4-cm-long 30-American-wire-gauge (AWG) copper wire (with radius 0.00423 λ at 10 GHz) was chosen as the thin-wire specimen. For the imaging measurements, the specimen was first centered in front of the aperture. Since the wire was cut to be near resonant length (roughly $\lambda/2$ at 10 GHz), this center positioning was accomplished by adjusting the specimen's placement while monitoring the peak $|S_{21}|$ as a function of frequency. A sample of such a signal is shown in Fig. 6. Once this peak was maximized, the wire was assumed centered in front of the aperture. It is interesting to note that it is already obvious that the near-field focusing effect predicted by both the MM and FDTD models is a real phenomenon. This is evident in Fig. 6 where the scattering parameter $|S_{21}|$ indicates that a larger signal is being received near resonance when the wire is centrally located between the aperture and the detector and *covers* the aperture.

After centering the 30-AWG wire, the aperture was scanned horizontally, while the wire specimen was scanned vertically. This image scan utilized 0.15-cm steps to form an 11×11 grid with the center of the wire corresponding to the center of the

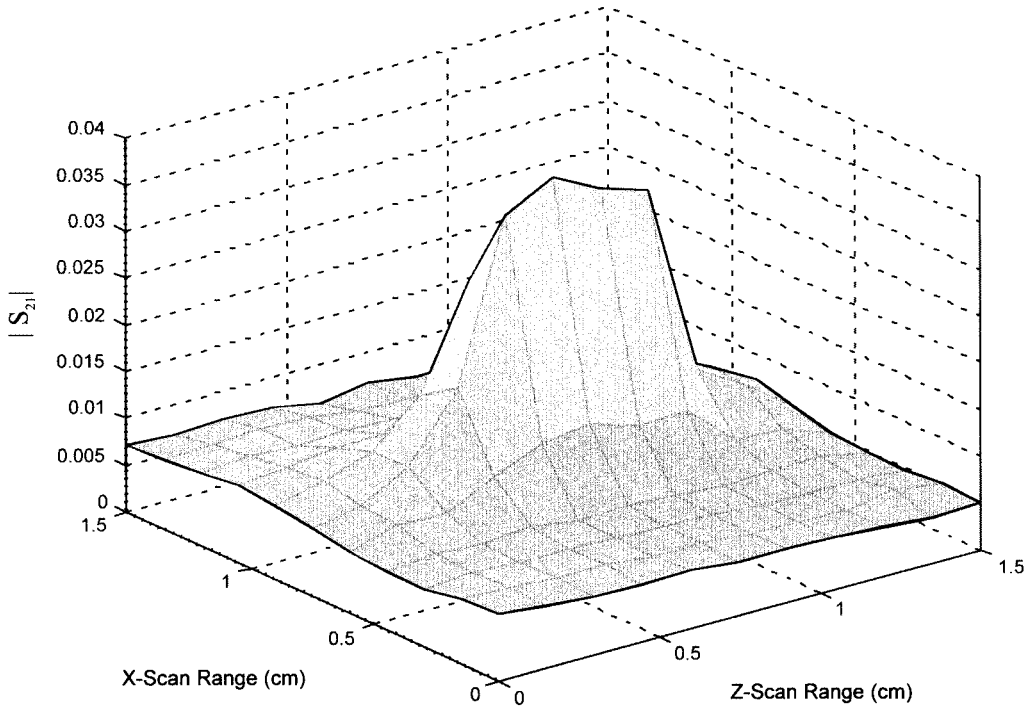

Fig. 7. Measured X-band NSMM image of a 30-AWG copper wire of length 1.4 cm and radius 0.0127 cm near its $\lambda/2$ resonance ($f = 9.63$ GHz)

image scan. Due to the frequency scanning capabilities of the VNA system, a complete spectrum from 8.2 to 12.5 GHz was collected at each "pixel" location with the VNA averaging function activated.

Of particular interest was the image collected at the resonant frequency. This resonant image was selected by first determining the frequency corresponding to the maximum value collected at the central pixel location. For our specimens, this frequency varied somewhere between 9–10 GHz depending on variations inherent in the specific specimen such as the length and radius of the wire. Once this frequency was determined, the signal at this frequency was selected for each spatial pixel location. In this manner, a complete image at the resonant frequency was produced, as shown in Fig. 7, for the 30-AWG wire.

In addition to the 30-AWG wire image, a second specimen consisting of a 1.3-cm-long 22-AWG wire (radius of 0.0107 λ at 10 GHz) was also used to produce a second NSMM image, shown in Fig. 8.

The images in Figs. 7 and 8 demonstrate two main points. First, it is evident that the signal strength increases when the wire is positioned between the aperture and detector, thereby validating the near-field focusing phenomenon predicted earlier by the MM and FDTD models. Second, the shape of the imaged wires also corroborates the computer models. Specifically, as the aperture is scanned along the length of the wires, the aperture–specimen coupling impedance along the wire varies, as demonstrated earlier in Fig. 3. In this manner, the increasing coupling impedance along the wire causes the rounded shape of the resonant images.

A third effect predicted by the computer models involved the incident field polarization. Both computer models predict that the image contrast is directly proportional to the field polarization, which is an obvious prediction for this thin-wire sample. When a linearly polarized $\overline{E}^i$ is oriented parallel to the wire, the highest contrast image (or strongest wire scattering) is obtained. As the polarization of the field is rotated perpendicular to the wire, the wire signal then diminishes considerably resulting in lower contrast images.

In order to test these predictions experimentally, three linearly polarized incident fields were chosen to obtain the cross-sectional images of an 18-AWG wire, as shown in Fig. 9. While the perpendicular- and parallel-polarized images were readily obtained, the image with $\overline{E}^i$ oriented approximately 45° to the wire proved more prone to error. Since the experimental setup did not readily allow the antennas to be rotated 45° without introducing measurement error, the wire itself was placed at approximately that angle in the Styrofoam holder. However, a precise angle was difficult to obtain due to the lack of rigidity in the Styrofoam. Furthermore, this approach also required both horizontal and vertical positioning systems to be utilized, thereby inducing more error. Consequently, the images are not completely accurate representations of exactly parallel, perpendicular, and 45° incident polarizations. Nevertheless, as predicted by the computer models, a general trend of diminishing contrast with polarization can still be observed in Fig. 9.

Incidentally, it should also be noted that these results indicate that, after being transmitted through the sub-wavelength aperture, the polarization of the incident plane wave is preserved in the near field.

IV. X-Band NSMM and Computer Simulation Comparisons

The data collected by the X-band NSMM instrument for the thin-wire specimens shown in the previous section appears to verify the results obtained by the computational models

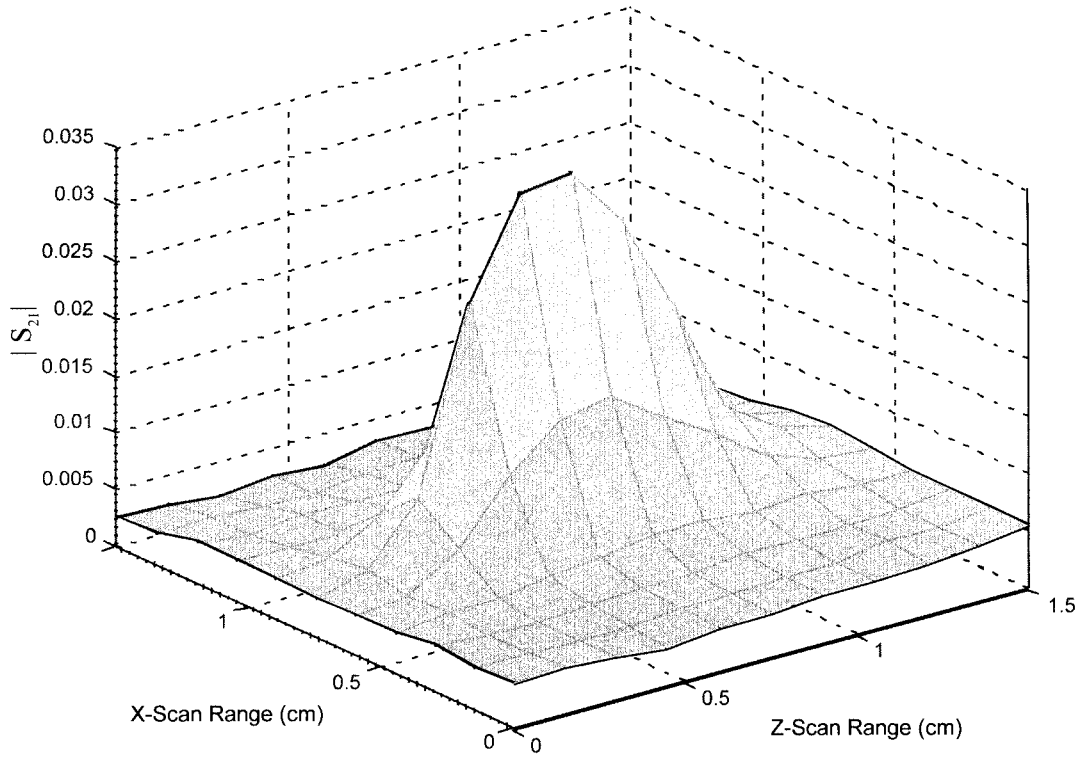

Fig. 8. Measured X-band NSMM image of a 22-AWG copper wire of length 1.3 cm and radius 0.0321 cm near its $\lambda/2$ resonance ($f = 9.77$ GHz)

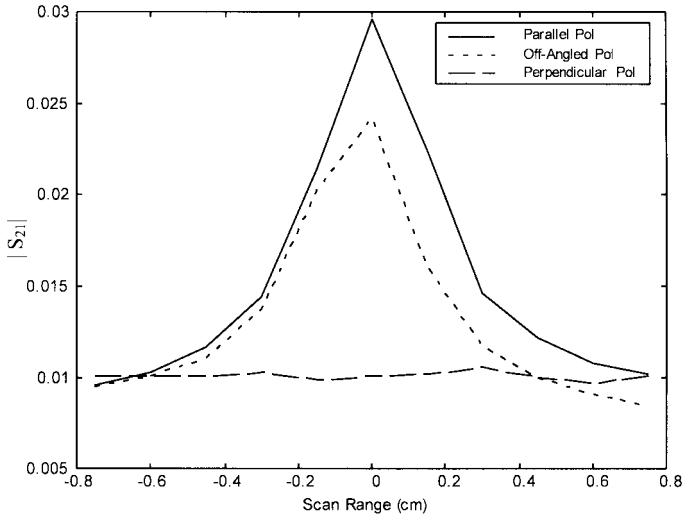

Fig. 9. Measured X-band NSMM images of an 18-AWG copper wire of length 1.2 cm and radius 0.0512 cm for varying field polarizations near the $\lambda/2$ resonance ($f = 10.5$ GHz). The center of the wire is located in the center of this plot

discussed earlier in this paper. Specifically, the near-field focusing effect, the polarization contrast relation, as well as the impedance-influenced image shape of the wire were verified. The question remains, however, just how accurate are the models.

In order to adequately answer this question, the X-band data was rigorously compared to the computer-generated data. While the X-band NSMM instrument implementation attempts to minimize sources of error, these sources are quite numerous and difficult to control. It is believed that the positioning of specimens relative to the aperture in all three dimensions is the greatest source of error. This positioning error includes the scanning movement, aperture–specimen separation distance, as well as the orientation of the specimen. Other sources of error include variations in wire length of the specimens. Additionally, due to the relatively small signal received, system noise and measurement errors also contribute to the overall error.

In order to minimize the error for these comparisons, two separate sets of data were collected. This proved to be necessary due to the inaccuracy inherent in the three-axis positioner. Overall, the most accurate scanning element of the X-band NSMM instrument is the micrometer driven stage that the plate is attached. Therefore, in order to utilize this stage exclusively for image scanning, cross-sectional images were first obtained across the wire for a vertically oriented wire, as illustrated in Figs. 1 and 5 (parallel to incident polarized field). This cross-sectional scan was followed by a second scan where cross-sectional images along the wire were obtained for a horizontally oriented wire. Since the field must be polarized such that it is oriented along the wire to produce the best images, both antennas were rotated 90° to match the orientation of the wires under investigation.

Five replicates of the 22-AWG wire were utilized. From this data, cross-sectional plots were produced, as seen in Figs. 10 and 11. In order to accurately compare the measure data to the computed data, all the data were normalized to eliminate differences due to varying source amplitudes. The measured X-band results indicate the mean value of the five replicates with error bars indicating the standard deviation. The mean value was utilized for these comparisons because of the fact that random errors average to zero with repeated measurements. Although the

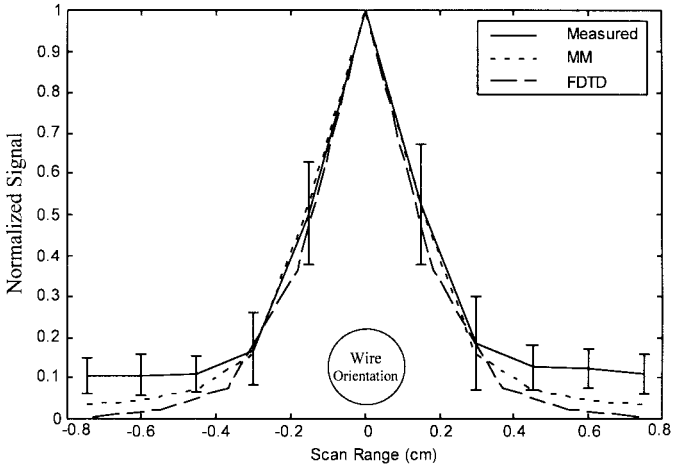

Fig. 10. Computed and measured NSMM images across a 22-AWG copper wire of length 1.3 cm and radius 0.0321 cm near the $\lambda/2$ resonance ($f = 9.77$ GHz). The center of the wire is located in the center of the plot, as indicated

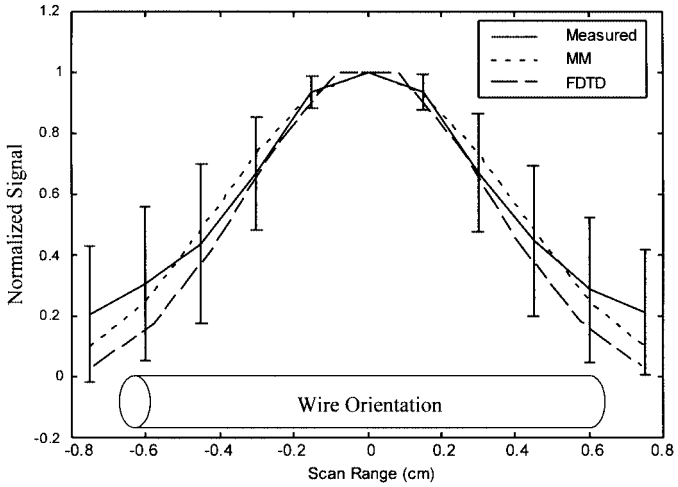

Fig. 11. Computed and measured NSMM images along the length of a 22-AWG copper wire of length 1.3 cm and radius 0.0321 cm near the $\lambda/2$ resonance ($f = 9.77$ GHz). The center of the wire is located in the center of the plot, as indicated

error bars are relatively large, indicating large variation of the data, the match for the mean is excellent. In fact, the wire itself matches extremely well with the largest discrepancy occurring at the ends of the scan, which indicates that this variation is due primarily to system noise.

V. Conclusions

The X-band NSMM instrument has demonstrated the validity of both the MM and FDTD models as valuable tools to characterize near-field imaging. Additionally, the X-band NSMM has also demonstrated previously unrecognized imaging phenomenon. Specifically, in addition to standard polarization effects and sub-wavelength imaging capabilities, the NSMM has also demonstrated both an impedance-based image shape effect, as well as a focusing effect for NSMM images. In this manner, the X-band NSMM has proven to be a valuable tool for comparing theoretical models with actual experimental results.

Acknowledgment

The authors acknowledge the valuable assistance of Dr. C. Buxton, Virginia Polytechnic Institute, Blacksburg, VA, in the development of the impedance model used to interpret the NSMM thin-wire images.

References

[1] M. A. Paesler and P. J. Moyer, *Near-Field Optics*. New York: Wiley, 1996.
[2] L. Novotony, D. W. Pohl, and P. Regli, "Light-propagation through nanometer-sized structures—the two-dimensional-aperture scanning near-field optical microscope," *J. Opt. Soc. Amer. A, Opt. Image Sci.*, vol. 11, no. 6, pp. 1768–1779, 1994.
[3] L. Novotony, D. W. Pohl, and B. Hecht, "Light confinement in scanning near-field optical microscopy," *Ultramicroscopy*, vol. 61, no. 1–4, pp. 1–9, 1995.
[4] E. Vasilyeva and A. Taflove, "Three dimensional modeling of amplitude-object imaging in scanning near-field optical microscopy," *Opt. Lett.*, vol. 23, no. 15, pp. 1155–1157, 1998.
[5] H. Furukawa and S. Kawata, "Local field enhancement with an apertureless near-field-microscope probe," *Opt. Commun.*, vol. 148, no. 4–6, pp. 221–224, 1998.
[6] E. Paule and P. Reineker, "Near-field optical microscopy: a numerical study of resolution and contrast," *J. Lumin.*, vol. 76–77, pp. 299–302, 1998.
[7] E. Betzig, M. Isaacsoln, H. Barshatzky, A. Lewis, and K. Lin, "Near field scanning optical microscopy (NSOM)," *Scanning Microscopy Technol. and Applicat.*, vol. 897, pp. 91–99, 1988.
[8] *2010 External Cavity Diode Laser Owner's Manual*, I. Newport Boulder Environmental Opt. Sens., Boulder, CO, 1998.
[9] E. Betzig, P. L. Finn, and J. S. Weiner, "Combined shear force and near-field scanning optical microscopy," *Appl. Phys. Lett.*, vol. 60, pp. 2484–2486, 1992.
[10] E. Betzig, J. K. Trautman, T. D. Harris, J. S. Weiner, and R. L. Kostelak, "Breaking the diffraction barrier: optical microscopy on a nanometric scale," *Science*, vol. 251, pp. 1468–1470, 1991.
[11] E. Betzig and J. K. Trautman, "Near-field optics: microscopy, spectroscopy, and surface modification beyond the diffraction limit," *Science*, vol. 257, pp. 189–195, 1992.
[12] R. F. Harrington, *Field Computation by Moment Methods*. Malabar, FL: Krieger, 1968.
[13] A. W. Glisson and D. R. Wilton, "Simple and efficient numerical methods for problems of electromagnetic radiation and scattering from surfaces," *IEEE Trans. Antennas Propagat.*, vol. AP-28, pp. 593–603, May 1980.
[14] C. A. Balanis, *Advanced Engineering Electromagnetics*. New York: Wiley, 1989.
[15] A. Roberts, "Probe-sample interaction in near-field microscopy: analysis of the interaction between a metal diffraction grating and a plane conductor," *Opt. Commun.*, vol. 98, pp. 225–230, 1993.
[16] S. Berntsen, E. Bozhevolnaya, and S. Bozhevolnyi, "Macroscopic self-consistent model for external-reflection near-field microscopy," *J. Opt. Soc. Amer. A, Opt. Image Sci.*, vol. 10, no. 5, pp. 878–885, 1993.
[17] A. F. Peterson, S. L. Ray, and R. Mittra, *Computational Methods for Electromagnetics*. Piscataway, NJ: IEEE Press, 1998.
[18] A. Taflove, *Computational Electrodynamics: The Finite-Difference Time-Domain*. Norwood, MA: Artech House, 1995.
[19] T. G. Jurgens and A. Taflove, "Three-dimensional contour FDTD modeling of scattering from single and multiple bodies," *IEEE Trans. Antennas Propagat.*, vol. 41, pp. 1703–1708, Dec. 1993.
[20] E. A. Ash and G. Nicholls, "Super-resolution aperture scanning microscope," *Nature*, vol. 237, pp. 510–511, 1972.
[21] T. Nozokido, J. Bae, and K. Mizuno, "Scanning near-field millimeter-wave microscopy using a metal slit as a scanning probe," *IEEE Trans. Microwave Theory Tech.*, vol. 49, pp. 491–499, Mar. 2001.
[22] K. W. Whites and C. Y. Chung, "Composite uniaxial bianisotropic chiral materials characterization: comparison of predicted and measured scattering," *J. Electromagn. Waves Applicat.*, vol. 11, pp. 371–394, 1997.

W. Charles Symons, III (S'94–M'95) received the B.S.E.E. degree from North Carolina State University, Raleigh, in 1992, and the M.S.E.E. and Ph.D. degrees from the University of Kentucky, Lexington, in 1995 and 1999, respectively.

He is currently a Visiting Assistant Professor with the Department of Electrical and Computer Engineering, Virginia Polytechnic Institute and State University, Blacksburg.

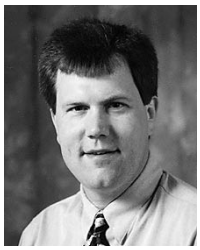

Keith W. Whites (S'84–M'86–SM'99) was born in Huron, SD. He received the B.S.E.E. degree from the South Dakota School of Mines and Technology, Rapid City, in 1986, and the M.S. and Ph.D. degrees from the University of Illinois at Urbana-Champaign, in 1988 and 1991, respectively.

In 1986, he was a Graduate Summer Assistant with Sandia National Laboratories, Livermore, CA. From 1987 to 1988, he was a Research Assistant with the U.S. Army Construction Engineering Research Laboratory (CERL), Champaign, IL. From 1988 to 1991, he held various fellowships and assistantships with the University of Illinois at Urbana-Champaign. From 1991 to 2001, he was an Assistant Professor and then an Associate Professor with the Department of Electrical and Computer Engineering, University of Kentucky. Since 2001, he has been with the South Dakota School of Mines and Technology, where he is currently a Professor and Steven P. Miller Chair in Electrical Engineering teaching courses in applied electromagnetics and wireless communications, among other topics. His current research interests include effective media calculations for complex composite materials, electromagnetic interaction with ultra-lightweight spacecraft including propulsion and control of solar sails, computational electromagnetics, equivalent boundary condition models, and homogenization of electromagnetics problems.

Dr. Whites is a member of Tau Beta Pi and Eta Kappa Nu. He was the 1999 recipient of the R. W. P. King Prize Paper Award presented by the IEEE Antennas and Propagation Society (IEEE AP-S) and the recipient of the National Science Foundation (NSF) Faculty Early Career Development (CAREER) and Research Initiation Awards.

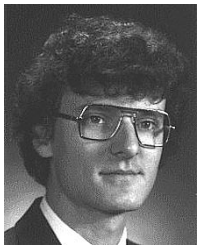

Robert A. Lodder received the B.S. degree (*cum laude*) in natural science and M.S. degree in chemistry from Xavier University, Cincinnati, OH, in 1981 and 1983, respectively, and the Ph.D. degree in analytical chemistry from Indiana University, Bloomington, in 1988, respectively.

He is currently an Associate Professor of pharmaceutical sciences with the College of Pharmacy, University of Kentucky Medical Center, University of Kentucky, Lexington. He holds a joint appointment with the Division of Analytical Chemistry, Department of Chemistry, University of Kentucky.

Dr. Lodder was the recipient of a First-Prize Award of the 1990 International IBM Supercomputing Competition, a National Science Foundation Young Investigator Award, the American Society of Agricultural Engineers (ASAE) Paper Award, a Buchi Near Infrared (NIR) Award, the Tomas Hirschfeld Award in Near-IR Spectroscopy, and a Research and Development 100 Award.